

# **Formation and manipulation of diatomic rotors at the symmetry-breaking surfaces of kagome superconductors**

Zihao Huang<sup>1,2#</sup>, Xianghe Han<sup>1,2#</sup>, Zhen Zhao<sup>1,2</sup>, Haitao Yang<sup>1,2</sup>, Hui Chen<sup>1,2\*</sup> and Hong-Jun Gao<sup>1,2\*</sup>

<sup>1</sup> *Beijing National Center for Condensed Matter Physics and Institute of Physics, Chinese Academy of Sciences, Beijing 100190, PR China*

<sup>2</sup> *School of Physical Sciences, University of Chinese Academy of Sciences, Beijing 100190, PR China*

## ABSTRACT

Artificial molecular rotors and motors hold great promise for functional nanomachines, but constructing diatomic rotors, crucial for these machines, is challenging due to surface constraints and limited chemical design. Here we report the construction of diatomic Cr-Cs and Fe-Cs rotors where a Cr or Fe atom revolves around a Cs atom at the Sb surface of the newly-discovered kagome superconductor CsV<sub>3</sub>Sb<sub>5</sub>. The rotation rate is controlled by bias voltage between the rotor and scanning tunneling microscope (STM) tip. The spatial distribution of rates exhibits C<sub>2</sub> symmetry, might linked to the symmetry-breaking charge orders of CsV<sub>3</sub>Sb<sub>5</sub>. We have expanded rotor construction to include different transition metals (Cr, Fe, V) and alkali metals (Cs, K). Remarkably, designed configurations of rotors are achieved through STM manipulation. Rotor orbits and quantum states are precisely controlled by tuning inter-rotor distance. Our findings establish a novel platform for the atomically precise fabrication of atomic motors on symmetry-breaking quantum materials, paving the way for advanced nanoscale devices.

**KEYWORDS:** *Diatomic rotor, atomic manipulation, nanomachine, scanning tunneling microscopy/spectroscopy, kagome superconductor*

The significance of nanoscale machines in diverse biological processes has spurred advancements in drug delivery, microelectronics, and the manipulation of nanoscale materials <sup>1-6</sup>. A pinnacle pursuit in molecular-scale engineering is the creation of artificial molecular machines capable of controlled mechanical motion and intricate tasks <sup>7-9</sup>. In recent years, the synthesis of various artificial molecular machines, such as molecular gears <sup>10</sup>, nanocars <sup>11</sup> and nanorobots <sup>5</sup>, has opened up extensive possibilities for the future of nanotechnology. While significant attention has been devoted to the design, construction, manipulation, and assembly of molecular rotors and motors as foundational components for nanomachines, the focus has primarily been on larger structures <sup>12-22</sup>. Quantum diatomic rotors, comprising only two atoms, represent the smallest building blocks and offer versatile potential for constructing various nanostructures through precise design and assembly. Theoretically, the rotational behavior of an H<sub>2</sub> molecule on a solid surface provides an ideal model for the elemental rotor. However, practical implementation has encountered limitations, particularly concerning rotational behaviors restricted to ortho-para conversion and the edges of metal surfaces <sup>23, 24</sup>. The construction of diatomic rotors, a crucial and challenging task in the realm of molecular rotors and nanomachines, remains largely unexplored.

In recent years, selecting functional quantum materials as substrate provides an effective strategy for the construction of new type surface-mounted rotors at molecular level. Compared with conditional noble metal substrates <sup>15</sup>, the quantum materials surface such as PdGa(111) <sup>25</sup>, Bi(111) <sup>26</sup> and carbon nanotube <sup>27</sup> exhibit symmetry-breaking non-trivial surface states or specific surface confinements, leading to a unconventional molecule-substrate interactions and the movements of molecular rotors. Such strategy also inspires the searching for diatomic rotor. Very recently, Desvignes *et al.* reported a diatomic rotor in Fe doped Bi<sub>2</sub>Se<sub>3</sub> where the atomically sized Fe defect embedded in the crystal structure <sup>28</sup>.

Here we report, for the first time, the construction of a Cr-Cs/ Fe-Cs diatomic rotor in a newly-discovered kagome superconductor CsV<sub>3</sub>Sb<sub>5</sub> <sup>29, 30</sup>, which has been reported to exhibit rich surface effects such as symmetry breaking orders <sup>31-36</sup>, carrier doping <sup>37, 38</sup> and polarity <sup>39</sup>. Using low-temperature scanning tunneling microscope (STM), we prove the diatomic nature of the rotors. The isolated alkali metal Cs atoms which originally stay at the Sb surface serves as the anchor, while the transition metal Cr/Fe atom that is evaporated onto the Sb surface traps into one Cs atom and rotate around the anchor. The anisotropic distribution of switching rates suggests the effects of symmetry breaking charge orders on the rotors. The rotation rate of the rotor changes as a function of bias voltage in the tunneling. We construct a series of diatomic rotors with various rotary properties by substituting the components of the diatomic rotors by other transition metals (such as Fe and V) or alkali metals (such as K). Remarkably, the rotation orbits

and rates are manipulated in atomic precision by placing the rotors in different motif. Our works provide a new platform for exploring and manufacturing atomic rotors and nanodevices in novel quantum materials.

The schematic of construction process of Cr-Cs diatomic rotor is presented in Figure 1(a). Following cleavage of  $\text{CsV}_3\text{Sb}_5$  at low temperature, Cs atoms exhibit diverse reconstructions on the as-cleaved surface<sup>40</sup>. As the externally-evaporated metal adatoms are difficult to be distinguished from the complex Cs reconstructions (Figure S1), we focus on the large-scale Sb terminated surface where the individual isolated Cs adatoms are randomly distributed (Figure S2). The Cr atoms are evaporated from the external metal sources onto the as-cleaved surface of  $\text{CsV}_3\text{Sb}_5$  (details see Method part). Upon evaporating Cr atom onto the Sb surface, certain Cr atoms capture isolated Cs adatoms, forming the “rotors” in the tunneling process, as schematically shown in Figure 1(a).

In the large-sized STM topographic image, the rotors exhibit wheel-like protrusions (marked by the red dotted circles) which are surrounded by the randomly distributed and isolated Cs atoms (Figure 1(b)). The close-up STM image shows that the wheel-like protrusion consists of an inner spherical center and an outer annulus orbit (Figure 1(c)). The inner spherical center shows a stable topographic feature with a diameter of approximately 1.1 nm, while the annulus orbit shows unstable height signal in the constant-current-mode STM images (Figure S3).

To reveal the atomic configuration of the rotor, we apply a tip pulse to tear the rotor apart<sup>13</sup>. As a result, the rotor divides into two distinct atoms with different sizes (Figure 1(d)). As the larger atom shares a similar diameter and height with the isolated Cs adatoms at the Sb surface (Figure S3), we attribute the larger atom to the Cs atom, while assign the smaller atom to the Cr atom. The tip-induced splitting of the rotor into two separated atoms is reversible. After pushing a Cr and a Cs atom closer by an STM tip, the Cs and Cr atoms recombine, re-establishing the rotor configuration (Figure 1(c), (d)).

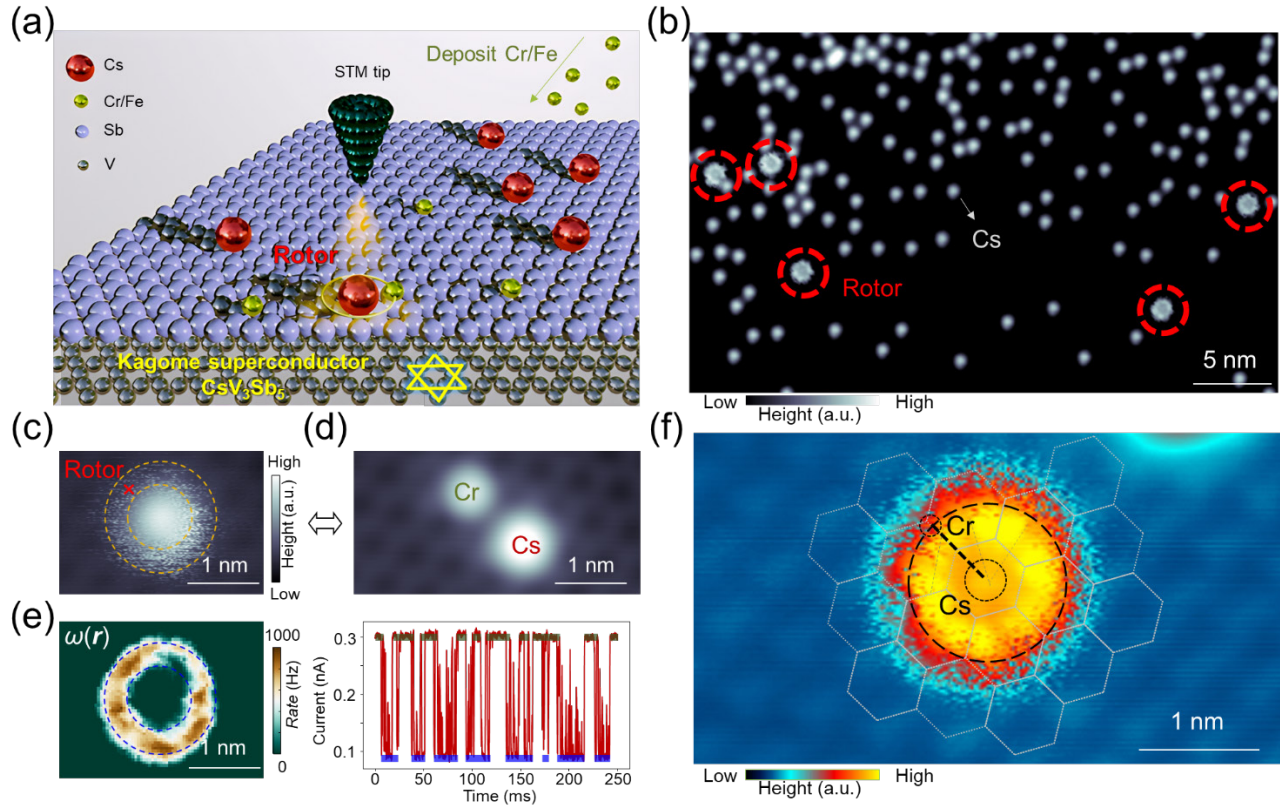


**Figure 1.** Construction of Cr-Cs diatomic rotors at the Sb surface of CsV<sub>3</sub>Sb<sub>5</sub> with diluted Cs adatoms. (a), Schematics of the formation of diatomic rotors. The Cr/Fe atom (marked by the yellow ball) distribute as a single atom and trap into a Cs atom (marked by the red ball) to form a diatomic rotor on the Sb surface of kagome superconductor CsV<sub>3</sub>Sb<sub>5</sub>. (b), STM images showing the Sb surface of CsV<sub>3</sub>Sb<sub>5</sub> crystal with dilute Cs atoms. The Cr-Cs diatomic rotors are highlighted by the red dotted circles ( $V_s = -500$  mV,  $I_t = 3$  nA). (c) - (d), The tip-induced separation of Cr-Cs rotors into a Cr and a Cs atom. Before separation, the Cr atom revolve around Cs atom forming a Cr-Cs rotor with an unstable annulus (c). After separation, the morphography of Cs and Cr atom are clearly visible (d).  $V_s = -500$  mV,  $I_t = 3$  nA. (e), Left: Rotation rate map  $\omega(r)$  of (c), showing that Cr atom rotates around Cs in a circular orbit ( $V = -600$  mV,  $I = 0.5$  nA). Right: The  $I-t$  spectrum measured at the annulus position (marked by the red cross) of Cr-Cs rotor in (c), showing steps-like feature with several discrete values ( $V = -250$  mV,  $I = 0.9$  nA). (f), Atomically-resolved STM topography of Cr-Cs diatomic rotor at the Sb surface of CsV<sub>3</sub>Sb<sub>5</sub>. The atomic model and Sb honeycomb lattice (white dotted hexagons) are overlaid in the image, showing that a Cr atom revolve around the Cs adatom ( $V_s = -500$  mV,  $I_t = 3$  nA).

We then investigate the rotatory nature of the rotor by monitoring the evolution of tunneling current over time ( $I$ - $t$  curve) at the annulus orbit part of the rotor while maintaining a constant tip height. The  $I$ - $t$  spectrum obtained at the annulus orbit exhibits cyclic jump sequences between two major current levels (right panel of Figure 1(e)), indicating that the rotor undergoes rotational switching between two unequal configurations. To study the spatial distribution of rotating features, we conduct the  $I$ - $t$  spectroscopic map (term as  $I(t, \mathbf{r})$ ) where  $I$ - $t$  curves are collected at each spatial spots within a selected region. We extract dominated rotating rate  $\omega$  by counting the current jump steps of  $I$ - $t$  spectra, which quantizes the rotational switching among the major quantum states (Figure S4). The rate map  $\omega(\mathbf{r})$  derived from the  $I$ - $t$  spectroscopic map  $I(t, \mathbf{r})$  illustrates that the rotating rates are notably high and primarily localized around the circular orbit region (left panel of Figure 1(e)).

We term the wheel-like protrusion in the STM image as a diatomic rotor, comprising simply two metal atoms, as depicted in Figure 1(f). The Cs atom positioned at the hexagonal center of Sb honeycomb lattice serves as an anchor, corresponding to the inner spherical center of wheel-like protrusion. The Cr atom rotates around the anchor along the axis within central Cs atom, forming a circular orbit region of the wheel-like protrusion.

To investigate the dynamics of the Cs-Cr diatomic rotor, we conduct the bias-dependent STM measurements of the Cr-Cs rotor. The topographic features undergo significant changes with the increasing sample bias (Figure 2(a) – (c)). At a low sample bias of -0.05 V, Cr-Cs rotors exhibit a 12-petals flower-shaped feature in the STM image (Figure 2(a)), suggesting 12 possible adsorption sites (Figure S5). With an increment in the sample bias, the topography of rotor gradually transforms into the wheel-like protrusion where annulus orbit become more unstable than those in low-bias STM images (Figure 2(b), (c)). It indicates that the switching rate of the diatomic rotor becomes larger with the increasing sample bias, which is further supported by the bias-dependent  $I$ - $t$  spectra (Figure 2(d)). When applying the low sample bias of -0.05 V, the  $I$ - $t$  curve acquired at the annulus orbit show no steps at the time scale of 250 ms, indicating a low switching rate. As the sample bias value increases (*e.g.* -0.2V and -0.6 V), the switching rates rise remarkably (Figure 2(d)). To reveal the evolution of the rate with the sample bias, we collect the  $I$ - $t$  spectroscopic maps  $I(t, \mathbf{r})$  on a diatomic Cr-Cs rotor at various scanning bias. At each sample bias, we carry out a statistical analysis of the rotating rate  $\omega$  extracted from the  $I(t, \mathbf{r})$  of rotor and get the spatial-averaged values  $\bar{\omega}$ , respectively. It clearly shows that the bias-dependent

$\bar{\omega}(V)$  exhibits a gap like feature where the rotating rate drops dramatically below a critical scanning bias  $\sim 0.2$  V. Such gap feature demonstrates an activation energy of the rotation switching of the Cr-Cs rotor from STM tip (Figure 2(e)). In addition, the bias-dependent behavior is not symmetric for the positive and negative sample bias, indicating the polar boosting effect by the electric field (Figure S6).

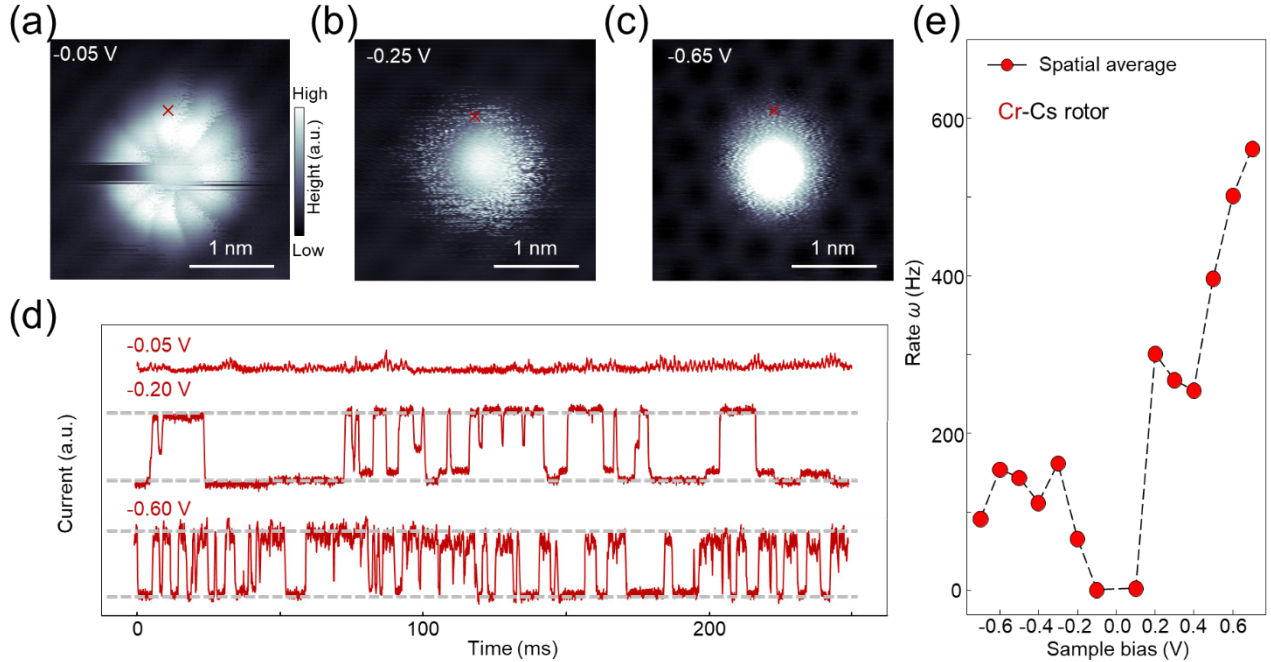


**Figure 2.** Bias-dependent rotational frequency of Cr-Cs rotors. The STM topography of a Cr-Cs rotor at sample bias of (a) -0.05 V, (b) -0.25 V and (c) -0.65 V, respectively, showing that the rotation switching of Cr atom gradually increases with larger sample bias ( $I=0.3$  nA). (d), The  $I-t$  spectra measured at the annulus position (red cross) of Cr-Cs rotor in (a) - (c). In the same period, the current steps change slow at small bias but jump fast at large bias ( $I=0.1$  nA). (e), The bias-dependent rotation switching rate  $\bar{\omega}(V)$  of Cr-Cs rotor, showing a bias gap where the rotor freezes inside the gap. The rotation switching rate  $\bar{\omega}(V)$  is spatially averaged over the rotor.

The formation of diatomic rotor is not limited by the Cr and Cs atoms but can be extended to other transition metal atoms and alkali metal atoms in the  $AV_3Sb_5$  system. For instance, we have deposited the Fe atoms onto Sb surface of  $CsV_3Sb_5$  with diluted Cs adatoms. The Fe adatoms capture the isolated Cs atoms on the Sb surface, giving rise to the formation of Fe-Cs diatomic rotors. The Fe-Cs rotors exhibit analogous features to the Cr-Cs rotors, identified as wheel-like protrusions in the STM image (Figure 3(a)). The rotating rate map  $\omega(\mathbf{r})$ , extracted from FT of  $I-t$  map, illustrates six sites with large switching rates in the annulus orbit region of Fe-Cs rotor (Figure 3(b)), namely six most unstable sites for Fe atoms. The  $I-t$  spectra at the annulus orbit of Fe-Cs rotor shows a step-like feature akin to the Cr-Cs rotor (Figure 3(c)). In addition, the bias-dependent mean rotating rate of Fe-Cs rotor  $\bar{\omega}(V)$  also exhibits a bias gap feature, indicating the activation energy of the rotation of Fe-Cs rotor from the STM tip (Figure 3(d) and Figure S7).

It is noticeable that the unidirectional  $4a_0$  charge stripe<sup>31-36</sup> (Figure S8(a)) in the Sb surface of  $CsV_3Sb_5$  can effectively tuning the distribution of switching rates of the rotors. The radially switching rates distributed anisotropic (Figure S8(b)) respective to the  $4a_0$  axis, suggesting the effects of symmetry breaking charge orders on rotors.

There are several notable distinctions between Fe-Cs and Cr-Cs rotors. Firstly, the range of current switching range is between -0.3 nA and -0.05 nA (Figure 3(c)), larger than that of Cr-Cs rotor (switching between -0.3 nA and -0.1 nA). Secondly, the bias gap size ( $\sim 0.2$  V) of Fe-Cs rotor is larger than that ( $\sim 0.1$  V) of Cr-Cs rotor. Finally, the  $\bar{\omega}(V)$  is more symmetric for positive and negative sample bias of Fe-Cs rotor (Figure S9), in contrast to the asymmetric feature observed in the Cr-Cs rotor. These distinctions might result from variations in adatom absorption and distinct bond strengths between adatoms and Cs atoms. Beyond the magnetic elements, we also deposit the non-magnetic V atoms onto the Sb surface of  $CsV_3Sb_5$  and  $KV_3Sb_5$  to construct V-Cs (Figure 3(e)) and V-K (Figure 3(f)) diatomic rotor, respectively. The universal formation of transition metal-alkali metal diatomic rotors provides a versatile platform to modulate rotating behaviors by selecting specific elements.



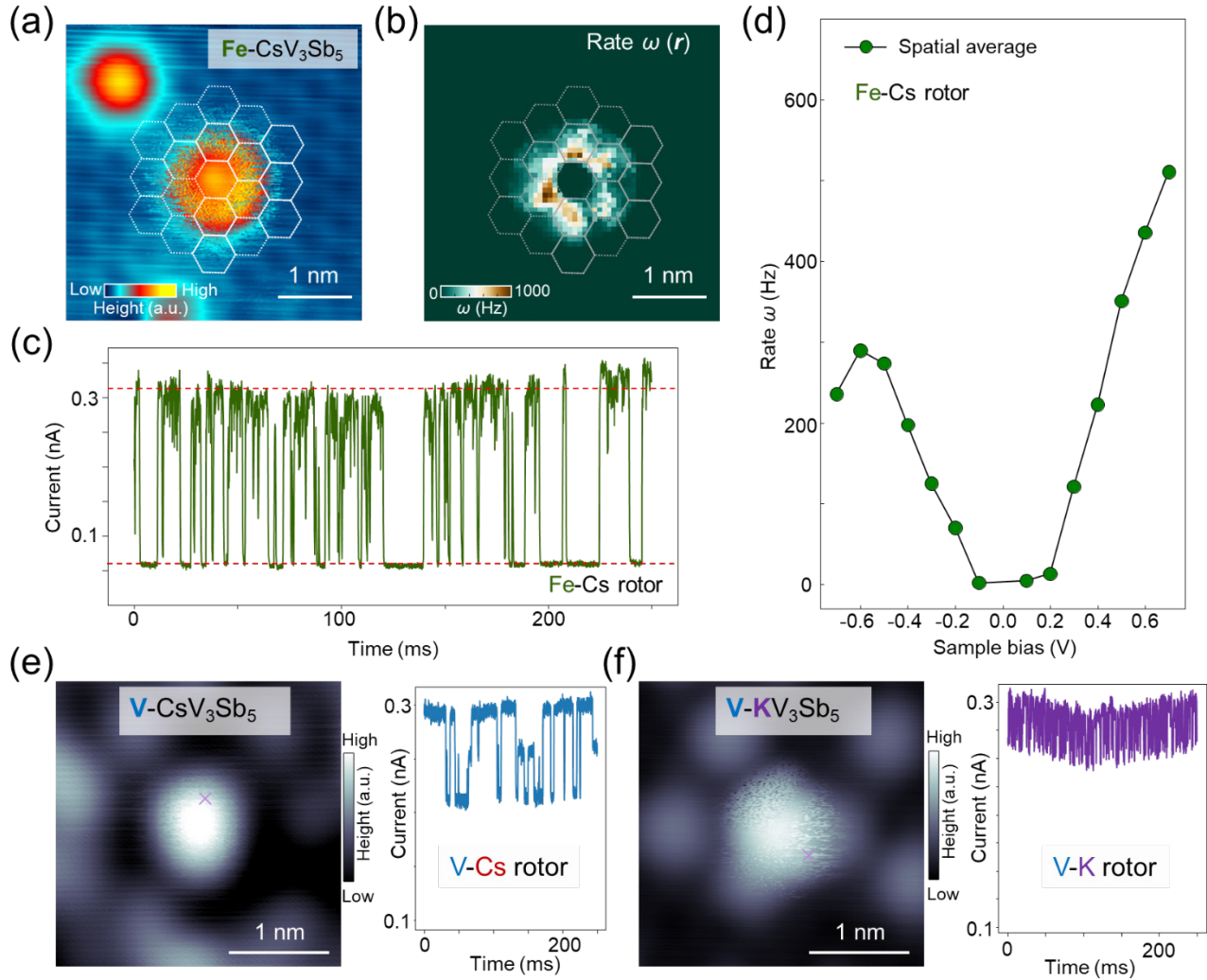


**Figure 3.** The formation of diatomic rotors in metal- $AV_3Sb_5$  ( $A=K, Cs$ ) system. (a), The STM topography of Fe-Cs rotors in  $CsV_3Sb_5$ . ( $V=-400$  mV,  $I=100$  pA). (b), Frequency map of (a), showing that Fe atom rotates around Cs in six most unstable sites ( $V=-400$  mV,  $I=100$  pA). (c), The  $I-t$  spectrum measured at the annulus position (red cross) of Fe-Cs rotor. ( $V=-600$  mV,  $I=0.3$  nA). (d), The bias-dependent frequency evolution of Fe-Cs rotor, showing a bias gap feature where the rotor freeze at small bias. The rotation switching rate  $\bar{\omega}(V)$  is spatially averaged over the rotor. (e), The STM topography (left) and  $I-t$  spectrum (right) of V-Cs rotors in  $CsV_3Sb_5$ . (Scan:  $V=-1$  V,  $I=20$  pA;  $I-t$ :  $V=-300$  mV,  $I=300$  pA). (f), The STM topography (left) and  $I-t$  spectrum (right) of V-K rotors in  $KV_3Sb_5$ . (Scan:  $V=-200$  mV,  $I=50$  pA;  $I-t$ :  $V=-300$  mV,  $I=300$  pA).

The atomically control over the rotational switching of diatomic rotors is achieved by directly manipulating and assembling them by an STM tip. The Cs atoms, serving as the anchor of diatomic rotor, are easily moved by the STM tip at low temperature<sup>35, 41</sup>. Consequently, the local position of a rotor at the Sb surface is atomically manipulated as well. During the STM manipulation process, we initially approach the STM tip closer to the surface and position it at one side of the rotor. The tip is then moved across the rotor and towards a selected spatial position. Maintaining the position of one rotor unchanged, we move another rotor closer, creating an artificial system for studying the rotating behaviors of two adjacent rotors. Initially, the distance between two rotors is  $3a_0$ , leaving the rotation rate of each rotor undisturbed (Figure 4(a)). As the two rotors approach each other closely ( $2a_0$ ), the central region hinders the rotary motion of the Fe atoms (Figure 4(b)), resulting in a stable  $I-t$  spectrum (Figure 4(d)). Moving even closer to a distance of  $a_0$ , the Fe atoms rotate around the two adjacent Cs atoms at much slower rates (Figure 4(c)) than a single rotor. Beyond the manipulation of two rotors, we achieve the assembly of the rotors into different motifs to modulate the rotating rates. For example, we assemble three rotors into a triangle pattern (Figure 4(e) – (g)) through step-by-step STM manipulations. When the distance between the rotors is far ( $\geq 3a_0$ ), the distribution of the rotation rates remains weakly affected (Figure 4(e), (f)). Moving closer to  $2a_0$ , Fe atoms are restricted from the center of triangular motif, resulting in a triangle orbit of rotation (Figure 4(g)). The weak van der Waals interaction between the rotors and substrates provides the opportunity to artificially design and build assembled rotational nanostructures atom by atom<sup>42, 43</sup>.

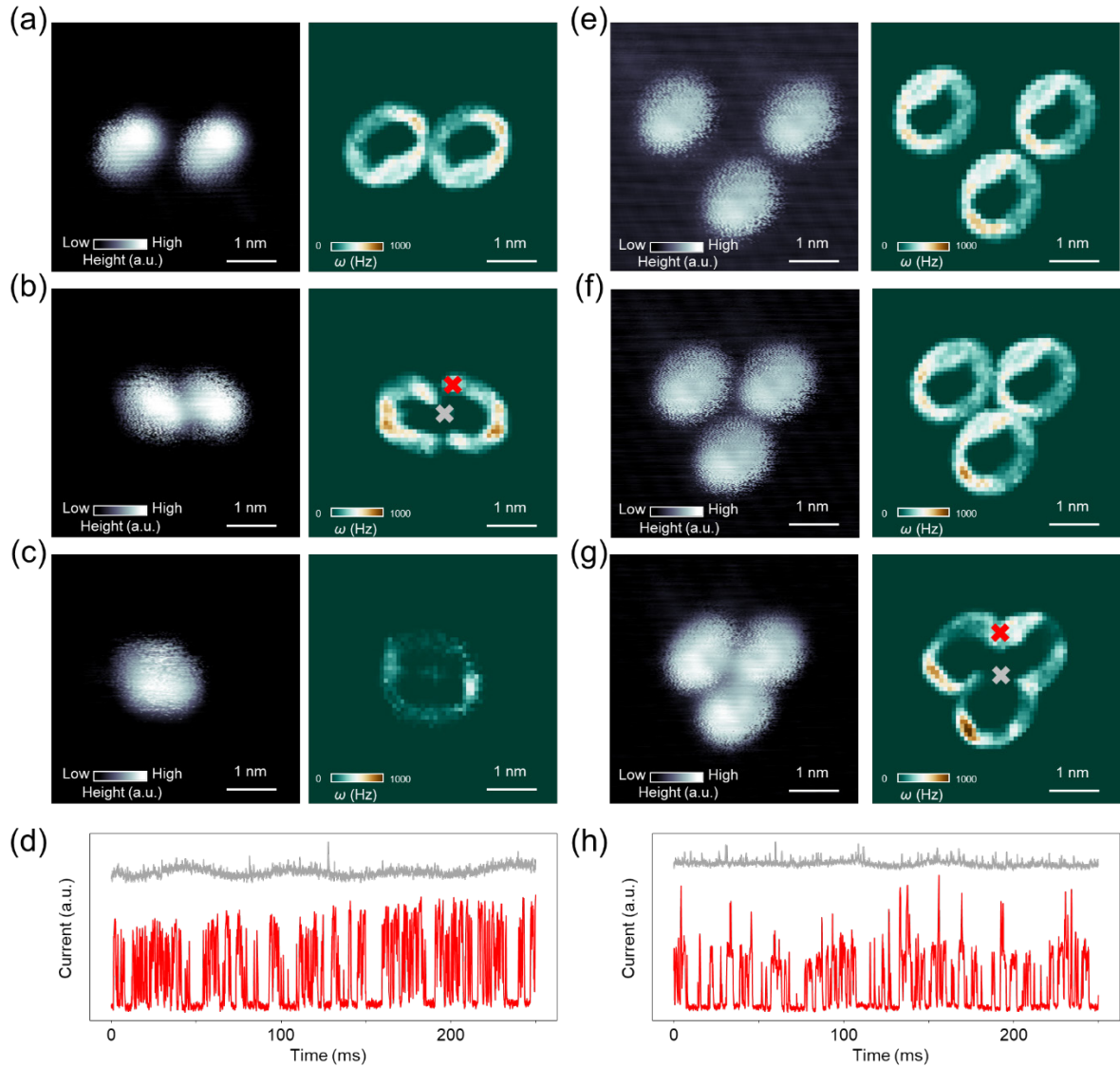


**Figure 4.** Atomically-engineering of Fe-Cs rotors by STM manipulation. (a), The STM topography (left panel) of two Fe-Cs rotors and their rates map (right panel). The distance between two rotors is  $3a_0$  ( $V=-400$  mV,  $I=100$  pA). (b), The STM topography (left panel) of two Fe-Cs rotors and their rates map (right panel). The distance between two rotors is  $2a_0$  ( $V=-400$  mV,  $I=100$  pA). (c), The STM topography (left panel) of two Fe-Cs rotors and their rates map (right panel). The distance between two rotors is  $a_0$  ( $V=-400$  mV,  $I=100$  pA). (d), The  $I-t$  spectra at the center (gray cross) and annulus (red cross) in (b), respectively, showing significant difference in rotating frequency. (e), The STM topography (left panel) of three Fe-Cs rotors and their rates map (right panel). The distance between the rotors is  $5a_0$  and  $4a_0$ , respectively ( $V=-400$  mV,  $I=100$  pA). (f), The STM topography (left panel) of three Fe-Cs rotors and their rates map (right panel). The distance between rotors is  $3a_0$  ( $V=-400$  mV,  $I=100$  pA). (g), The STM topography (left panel) of three Fe-Cs rotors and their rates map (right panel). The distance between rotors is  $2a_0$  ( $V=-400$  mV,  $I=100$  pA). (h), The  $I-t$  spectra at the center (gray cross) and annulus (red cross) in (g), respectively, showing significant difference in rotating frequency.

The realization of diatomic rotors introduces a novel paradigm for the design and construction of building blocks crucial for functional nanomachines and the future landscape of nanotechnology. The inherent simplicity of diatomic rotors marks the inception of atomic machines, serving as fundamental components for more intricate nano-machinery. The diatomic rotors consist of magnetic elements implicate the applications in the nanoscale robots based on spintronics. Furthermore, the electrical controllability of the on/off rate in diatomic rotors opens avenues for potential electrical applications. The symmetry-breaking rotation switching of the rotor probably correlate to the symmetry breaking charge orders<sup>34</sup> in the kagome superconductors, which provides possibilities to tune the electronic states of the rotors by the degrees of charges. Substituting atoms within the diatomic rotors allows for the tuning of their quantum properties, establishing a novel platform for exploring two-body quantum interactions. The discovery is poised to propel advancements in the design of functional and automated nanomachinery, particularly those capable of operation on material surfaces<sup>8</sup>. The potential for tuning quantum properties and leveraging electronic control underscores the versatility of diatomic rotors as foundational elements for emerging nanotechnological applications.

## EXPERIMENTAL METHOD

**Sample preparation.** Single crystals of  $\text{CsV}_3\text{Sb}_5$  and  $\text{KV}_3\text{Sb}_5$  were grown *via* a modified self-flux method<sup>35</sup>. The samples used in the STM/S experiments are cleaved *in situ* at low temperature (13 K) and immediately transferred to an STM chamber. Cr, Fe and V were *in situ* evaporated from pure metal rods (purity of 99.99%) using a commercial electron beam evaporator and deposited onto the surface of the  $\text{CsV}_3\text{Sb}_5$  with a substrate temperature of  $\sim 20$  K.

**Scanning tunneling microscopy/spectroscopy.** Experiments were performed in an ultrahigh vacuum ( $1 \times 10^{-10}$  mbar) ultra-low temperature STM system equipped with 11 T magnetic field. Non-superconducting tungsten tips were fabricated via electrochemical etching and calibrated on a clean Au(111) surface prepared by repeated cycles of sputtering with argon ions and annealing at 500 °C. STM topographic images are acquired in constant-current mode, with all the scanning parameters (setpoint voltage  $V_s$  and current  $I_t$ ) listed in the figure captions. Unless otherwise noted, the  $dI/dV$  spectra were acquired in constant-height mode by a standard lock-in amplifier at a modulation frequency of 973.1 Hz. Current–time ( $I-t$ ) curves, for measuring the occupation probability of adjacent rotational configurations of the diatomic rotors, were acquired at a selected spatial spot with the feedback loop closed. The  $I-t$  map  $I(\mathbf{r}, t)$  were acquired in constant-height mode where the  $I-t$  curves were collected at each spatial spots of the map. The frequency map  $f(\mathbf{r})$  was obtained by extracting the frequency value  $f$  from the  $I-t$  curves in each spatial spot of the  $I-t$  map by counting the step changing (details are shown in Figure S4).

## **AUTHOR INFORMATION**

### **Corresponding Authors**

**Hui Chen** [hchenn04@iphy.ac.cn](mailto:hchenn04@iphy.ac.cn),

**Hong-Jun Gao** [hjgao@iphy.ac.cn](mailto:hjgao@iphy.ac.cn)

## REFERENCES

- (1) Toumey, C. From nano machines to Nobel prizes. *Nat. Nanotechnol.* **2017**, *12* (1), 1-1. DOI:10.1038/nano.2016.289.
- (2) Zhao, J. H.; Benlekbir, S.; Rubinstein, J. L. Electron cryomicroscopy observation of rotational states in a eukaryotic V-ATPase. *Nature* **2015**, *521* (7551), 241-245. DOI: 10.1038/nature14365.
- (3) Erbas-Cakmak, S.; Leigh, D. A.; McTernan, C. T.; Nussbaumer, A. L. Artificial Molecular Machines. *Chem. Rev.* **2015**, *115* (18), 10081-10206. DOI: 10.1021/acs.chemrev.5b00146.
- (4) Finnigan, G. C.; Hanson-Smith, V.; Stevens, T. H.; Thornton, J. W. Evolution of increased complexity in a molecular machine. *Nature* **2012**, *481* (7381), 360-U143. DOI: 10.1038/nature10724.
- (5) Lund, K.; Manzo, A. J.; Dabby, N.; Michelotti, N.; Johnson-Buck, A.; Nangreave, J.; Taylor, S.; Pei, R. J.; Stojanovic, M. N.; Walter, N. G.; et al. Molecular robots guided by prescriptive landscapes. *Nature* **2010**, *465* (7295), 206-210. DOI: 10.1038/nature09012.
- (6) Browne, W. R.; Feringa, B. L. Making molecular machines work. *Nat. Nanotechnol.* **2006**, *1* (1), 25-35. DOI: 10.1038/nano.2006.45.
- (7) Filatov Gulak, M.; Paolino, M.; Pierron, R.; Cappelli, A.; Giorgi, G.; Leonard, J.; Huix-Rotllant, M.; Ferre, N.; Yang, X.; Kaliakin, D.; et al. Towards the engineering of a photon-only two-stroke rotary molecular motor. *Nat. Commun.* **2022**, *13* (1), 6433. DOI: 10.1038/s41467-022-33695-x.
- (8) Dattler, D.; Fuks, G.; Heiser, J.; Moulin, E.; Perrot, A.; Yao, X. Y.; Giuseppone, N. Design of Collective Motions from Synthetic Molecular Switches, Rotors, and Motors. *Chem. Rev.* **2020**, *120* (1), 310-433. DOI: 10.1021/acs.chemrev.9b00288.
- (9) Roke, D.; Wezenberg, S. J.; Feringa, B. L. Molecular rotary motors: Unidirectional motion around double bonds. *P. Natl. Acad. Sci. USA* **2018**, *115* (38), 9423-9431. DOI: 10.1073/pnas.1712784115.
- (10) Manzano, C.; Soe, W. H.; Wong, H. S.; Ample, F.; Gourdon, A.; Chandrasekhar, N.; Joachim, C. Step-by-step rotation of a molecule-gear mounted on an atomic-scale axis. *Nat. Mater.* **2009**, *8* (7), 576-579. DOI: 10.1038/nmat2467.
- (11) Chu, P. L. E.; Wang, L. Y.; Khatua, S.; Kolomeisky, A. B.; Link, S.; Tour, J. M. Synthesis and Single-Molecule Imaging of Highly Mobile Adamantane-Wheeled Nanocars. *ACS Nano* **2013**, *7* (1), 35-41. DOI: 10.1021/nm304584a.
- (12) Ajayi, T. M.; Singh, V.; Latt, K. Z.; Sarkar, S.; Cheng, X.; Premarathna, S.; Dandu, N. K.; Wang, S.; Movahedifar, F.; Wieghold, S.; et al. Atomically precise control of rotational dynamics in charged rare-earth complexes on a metal surface. *Nat. Commun.* **2022**, *13* (1), 6305. DOI: 10.1038/s41467-022-33897-3.
- (13) Larson, A. M.; Groden, K.; Hannagan, R. T.; McEwen, J. S.; Sykes, E. C. H. Understanding Enantioselective Interactions by Pulling Apart Molecular Rotor Complexes. *ACS Nano* **2019**, *13* (5), 5939-5946. DOI: 10.1021/acsnano.9b01781.
- (14) Stacko, P.; Kistemaker, J. C. M.; van Leeuwen, T.; Chang, M. C.; Otten, E.; Feringa, B. L. Locked synchronous rotor motion in a molecular motor. *Science* **2017**, *356* (6341), 964-968. DOI: 10.1126/science.aam8808.
- (15) Barth, J. V. Molecular architectonic on metal surfaces. *Annu. Rev. Phys. Chem.* **2007**, *58*, 375-407. DOI: 10.1146/annurev.physchem.56.092503.141259.
- (16) Lu, H. L.; Cao, Y.; Qi, J.; Bakker, A.; Strassert, C. A.; Lin, X.; Ernst, K. H.; Du, S.; Fuchs, H.; Gao, H. J. Modification of the Potential Landscape of Molecular Rotors on Au(111) by the Presence of an STM Tip. *Nano Lett.* **2018**, *18* (8), 4704-4709. DOI: 10.1021/acs.nanolett.8b01019.
- (17) Grill, L.; Rieder, K. H.; Moresco, F.; Rapenne, G.; Stojkovic, S.; Bouju, X.; Joachim, C. Rolling a single molecular wheel at the atomic scale. *Nat. Nanotechnol.* **2007**, *2* (2), 95-98. DOI: 10.1038/nano.2006.210.

- (18) Kim, H. W.; Han, M.; Shin, H. J.; Lim, S.; Oh, Y.; Tamada, K.; Hara, M.; Kim, Y.; Kawai, M.; Kuk, Y. Control of molecular rotors by selection of anchoring sites. *Phys. Rev. Lett.* **2011**, *106* (14), 146101. DOI: 10.1103/PhysRevLett.106.146101.
- (19) Tabe, Y.; Yokoyama, H. Coherent collective precession of molecular rotors with chiral propellers. *Nat. Mater.* **2003**, *2* (12), 806-809. DOI: 10.1038/nmat1017.
- (20) Gao, L.; Liu, Q.; Zhang, Y. Y.; Jiang, N.; Zhang, H. G.; Cheng, Z. H.; Qiu, W. F.; Du, S. X.; Liu, Y. Q.; Hofer, W. A.; et al. Constructing an Array of Anchored Single-Molecule Rotors on Gold Surfaces. *Phys. Rev. Lett.* **2008**, *101* (19). DOI: ARTN 19720910.1103/PhysRevLett.101.197209.
- (21) Simpson, G. J.; Persson, M.; Grill, L. Adsorbate motors for unidirectional translation and transport. *Nature* **2023**, *621* (7977), 82-86. DOI: 10.1038/s41586-023-06384-y.
- (22) Cao, Y.; Mieres-Perez, J.; Rowen, J. F.; Sanchez-Garcia, E.; Sander, W.; Morgenstern, K. Chirality control of a single carbene molecule by tip-induced van der Waals interactions. *Nature Communications* **2023**, *14* (1), 4500. DOI: 10.1038/s41467-023-39870-y.
- (23) Svensson, K.; Bengtsson, L.; Bellman, J.; Hassel, M.; Persson, M.; Andersson, S. Two-Dimensional Quantum Rotation of Adsorbed H<sub>2</sub>. *Phys. Rev. Lett.* **1999**, *83* (1), 124-127. DOI: 10.1103/PhysRevLett.83.124.
- (24) Bengtsson, L.; Svensson, K.; Hassel, M.; Bellman, J.; Persson, M.; Andersson, S. H<sub>2</sub> adsorbed in a two-dimensional quantum rotor state on a stepped copper surface. *Phys. Rev. B* **2000**, *61* (24), 16921-16932. DOI: 10.1103/PhysRevB.61.16921.
- (25) Stolz, S.; Groning, O.; Prinz, J.; Brune, H.; Widmer, R. Molecular motor crossing the frontier of classical to quantum tunneling motion. *Proc. Natl. Acad. Sci.* **2020**, *117* (26), 14838-14842. DOI: 10.1073/pnas.1918654117.
- (26) Sun, K.; Tao, M. L.; Tu, Y. B.; Wang, J. Z. Off-Center Rotation of CuPc Molecular Rotor on a Bi(111) Surface and the Chiral Feature. *Molecules* **2017**, *22* (5). DOI: 10.3390/molecules22050740.
- (27) Cai, K.; Yu, J. Z.; Wan, J.; Yin, H.; Shi, J.; Qin, Q. H. Configuration jumps of rotor in a nanomotor from carbon nanostructures. *Carbon* **2016**, *101*, 168-176. DOI: 10.1016/j.carbon.2016.01.089.
- (28) Desvignes, L.; Stolyarov, V. S.; Aprili, M.; Masee, F. Tunable High Speed Atomic Rotor in Bi<sub>2</sub>Se<sub>3</sub> Revealed by Current Noise. *ACS Nano* **2021**, *15* (1), 1421-1425. DOI: 10.1021/acsnano.0c08718.
- (29) Chen, H.; Hu, B.; Ye, Y.; Yang, H.; Gao, H.-J. Superconductivity and unconventional density waves in vanadium-based kagome materials AV<sub>3</sub>Sb<sub>5</sub>. *Chin. Phys. B* **2022**, *31* (9), 097405. DOI: 10.1088/1674-1056/ac7f95.
- (30) Neupert, T.; Denner, M. M.; Yin, J.-X.; Thomale, R.; Hasan, M. Z. Charge order and superconductivity in kagome materials. *Nat. Phys.* **2022**, *18* (2), 137-143. DOI: 10.1038/s41567-021-01404-y.
- (31) Nie, L.; Sun, K.; Ma, W.; Song, D.; Zheng, L.; Liang, Z.; Wu, P.; Yu, F.; Li, J.; Shan, M.; et al. Charge-density-wave-driven electronic nematicity in a kagome superconductor. *Nature* **2022**, *604*, 59-64. DOI: 10.1038/s41586-022-04493-8.
- (32) Guo, C.; Putzke, C.; Konyzheva, S.; Huang, X.; Gutierrez-Amigo, M.; Errea, I.; Chen, D.; Vergniory, M. G.; Felser, C.; Fischer, M. H.; et al. Switchable chiral transport in charge-ordered kagome metal CsV<sub>3</sub>Sb<sub>5</sub>. *Nature* **2022**. DOI: 10.1038/s41586-022-05127-9.
- (33) Li, H.; Zhao, H.; Ortiz, B. R.; Park, T.; Ye, M.; Balents, L.; Wang, Z.; Wilson, S. D.; Zeljkovic, I. Rotation symmetry breaking in the normal state of a kagome superconductor KV<sub>3</sub>Sb<sub>5</sub>. *Nat. Phys.* **2022**, 265-270. DOI: 10.1038/s41567-021-01479-7.
- (34) Jiang, Y.-X.; Yin, J.-X.; Denner, M. M.; Shumiya, N.; Ortiz, B. R.; Xu, G.; Guguchia, Z.; He, J.; Hossain, M. S.; Liu, X.; et al. Unconventional chiral charge order in kagome superconductor KV<sub>3</sub>Sb<sub>5</sub>. *Nat. Mater.* **2021**, *20*, 1353-1357. DOI: 10.1038/s41563-021-01034-y.



- (35) Chen, H.; Yang, H.; Hu, B.; Zhao, Z.; Yuan, J.; Xing, Y.; Qian, G.; Huang, Z.; Li, G.; Ye, Y.; et al. Roton pair density wave in a strong-coupling kagome superconductor. *Nature* **2021**, *599* (7884), 222-228. DOI: 10.1038/s41586-021-03983-5.
- (36) Zhao, H.; Li, H.; Ortiz, B. R.; Teicher, S. M. L.; Park, T.; Ye, M.; Wang, Z.; Balents, L.; Wilson, S. D.; Zeljkovic, I. Cascade of correlated electron states in the kagome superconductor CsV<sub>3</sub>Sb<sub>5</sub>. *Nature* **2021**, *599* (7884), 216-221. DOI: 10.1038/s41586-021-03946-w.
- (37) Yu, J.; Xu, Z.; Xiao, K.; Yuan, Y.; Yin, Q.; Hu, Z.; Gong, C.; Guo, Y.; Tu, Z.; Tang, P.; et al. Evolution of electronic structure in pristine and Rb-reconstructed surfaces of kagome metal RbV<sub>3</sub>Sb<sub>5</sub>. *Nano Lett.* **2022**, *22* (3), 918-925. DOI: 10.1021/acs.nanolett.1c03535.
- (38) Nakayama, K.; Li, Y.; Kato, T.; Liu, M.; Wang, Z.; Takahashi, T.; Yao, Y.; Sato, T. Carrier injection and manipulation of charge-density wave in kagome superconductor CsV<sub>3</sub>Sb<sub>5</sub>. *Phys. Rev. X* **2022**, *12* (1), 011001. DOI: 10.1103/PhysRevX.12.011001.
- (39) Kato, T.; Li, Y.; Nakayama, K.; Wang, Z.; Souma, S.; Kitamura, M.; Horiba, K.; Kumigashira, H.; Takahashi, T.; Sato, T. Polarity-dependent charge density wave in the kagome superconductor CsV<sub>3</sub>Sb<sub>5</sub>. *Phys. Rev. B* **2022**, *106* (12), L121112. DOI: 10.1103/PhysRevB.106.L121112.
- (40) Yu, J.; Xu, Z.; Xiao, K.; Yuan, Y.; Yin, Q.; Hu, Z.; Gong, C.; Guo, Y.; Tu, Z.; Tang, P. J. N. L. Evolution of electronic structure in pristine and Rb-reconstructed surfaces of kagome metal RbV<sub>3</sub>Sb<sub>5</sub>. **2022**, *22* (3), 918-925.
- (41) Hu, B.; Ye, Y.; Huang, Z.; Han, X.; Zhao, Z.; Yang, H.; Chen, H.; Gao, H.-J. Robustness of the unidirectional stripe order in the kagome superconductor CsV<sub>3</sub>Sb<sub>5</sub>. *Chin. Phys. B* **2022**, *31* (5), 058102. DOI: 10.1088/1674-1056/ac5888.
- (42) Stilp, F.; Bereczuk, A.; Berwanger, J.; Mundigl, N.; Richter, K.; Giessibl, F. J. Very weak bonds to artificial atoms formed by quantum corrals. *Science* **2021**, *372*, 1196.
- (43) Khajetoorians, A. A.; Wegner, D.; Otte, A. F.; Swart, I. Creating designer quantum states of matter atom-by-atom. *Nat. Rev. Phys.* **2019**, *1* (12), 703-715. DOI: 10.1038/s42254-019-0108-5.